Computers and Structures 152 (2015) 11–26

Contents lists available at ScienceDirect

Computers and Structures

journal homepage: www.elsevier.com/locate/compstruc

An extended finite element model for modelling localised fracture of reinforced concrete beams in fire

Feiyu Liao *, Zhaohui Huang

Department of Mechanical, Aerospace and Civil Engineering, College of Engineering, Design and Physical Sciences, Brunel University, Uxbridge, Middlesex UB8 3PH, UK

ARTICLE INFO

Article history:
Received 30 April 2014
Accepted 8 February 2015
Available online 3 March 2015

Keywords:
Localised crack
Reinforced concrete beams in fire
Extended finite element method (XFEM)
Layered concrete element
Crack opening

ABSTRACT

A robust finite element procedure for modelling the localised fracture of reinforced concrete beams at elevated temperatures is developed. In this model a reinforced concrete beam is represented as an assembly of 4-node quadrilateral plain concrete, 3-node main reinforcing steel bar, and 2-node bond-link elements. The concrete element is subdivided into layers for considering the temperature distribution over the cross-section of a beam. An extended finite element method (XFEM) has been incorporated into the concrete elements in order to capture the localised cracks within the concrete. The model has been validated against previous fire test results on the concrete beams.

1. Introduction

Localised fracture of reinforced concrete members has recently been of interest to many researchers and engineers. Under fire conditions, reinforced concrete structural members (such as beams or slabs) are often forced into high deformation. This results in the formation of large individual cracks within the members, which has been observed in previous experimental tests [1–3]. These large individual cracks influence the exposure condition of the reinforcing steel bar to the fire. In some cases the steel reinforcements are directly exposed to fire, whereby significantly reducing the fire resistance of the structures. In some extreme cases, localised large cracks could even result in integrity failure of the structures [1–3]. A key factor in assessing the fire resistance of the structures is through predicting the localised fracture of their structural members. Recently, the performance-based approach has been used in the fire safety design of reinforced concrete structures, which requires the use of accurate numerical models for predicting the response of structural members in fire. In the past two decades, plenty of numerical simulations and analyses have been conducted for modelling concrete structures at elevated temperatures [4–14]. Those studies were all based on the continuum approach, in which smeared cracking was adopted to simulate the cracks within concrete members. Existing research indicates that models based on smeared cracking can predict global responses, such as deflection and structural stability, with reasonable accuracy. However, the smeared cracking model cannot capture the localised fracture within structural members, and quantitatively predict crack openings. As far as performance-based fire safety design is concerned, predicting the opening of individual cracks at critical sections of critical members can be a crucial issue when evaluating the reliability of structures under fire conditions. Little research has yet been done on modelling localised fractures for reinforced concrete structural members under fire conditions.

In the past, a discrete-cracking model has been used successfully for modelling the formation and propagation of cracks in structural members, when the crack path is known in advance. However, this approach has to limit the cracks to inter-element boundaries, which might cause mesh bias, or requires performing costly re-meshing during the analysis process. To model individual cracks more effectively, the extended finite element method (XFEM) was introduced [15,16], based on the partition of unity theory [17]. The XFEM approaches in conjunction with cohesive-zone models [18–21] allow displacement jumps within conventional finite elements to analyse localisation and fracture in engineering materials. In the last decade, the XFEM has been successfully extended to many applications, such as multiple cracks in brittle materials, intersecting cracks and dynamic crack growth [22–26]. In terms of computer implementation of enriched finite element methods, a general structure for an object-oriented enriched finite element code (the XFEM library) was presented by [27], which had been designed to meet all natural requirements for modularity, extensibility, and robustness. Another open-source software framework called PERMIX for multiscale modelling of material

* Corresponding author at: College of Transportation and Civil Engineering, Fujian Agriculture and Forestry University, Fuzhou 350002, PR China.
E-mail address: Feiyu.Liao@brunel.ac.uk (F. Liao).

http://dx.doi.org/10.1016/j.compstruc.2015.02.006
0045-7949/

NOTATION

$\mathbf{B}^{u}_{sta}$	regular strain–displacement transformation matrix
$\mathbf{B}^{a}_{enr}$	enhanced strain–displacement transformation matrix
$\mathbf{D}$	material constitutive matrix of plain concrete
$\mathbf{f}^{int}$	element internal force vector
$\mathbf{f}^{int}_{a}$	enhanced element internal force vector
$\mathbf{f}^{int}_{u}$	regular element internal force vector
$\mathbf{f}^{int}_{\Gamma}$	element internal force vector corresponding to traction
G_f	fracture energy of concrete
$\mathbf{K}_{aa}$	enhanced element stiffness matrix
$\mathbf{K}_{uu}$	regular element stiffness matrix
$\mathbf{K}_{\Gamma}$	element stiffness matrix corresponding to traction
$\mathbf{T}_a$	tangent stiffness of traction–separation relation
$\mathbf{t}_a$	traction within the cracks
$sign(x)$	sign function
$\mathbf{u}_{\text{cont}}$	vector of continuous displacement field
$\mathbf{u}_{\text{dis}}$	vector of discontinuous displacement field
$\Psi_i(\mathbf{x})$	enhancement function

failure was presented by [28]. The integration method for the XFEM based on Schwarz–Christoffel mappings was proposed by [29] to simplify the numerical integration on arbitrary polygonal domains. The application of strain smoothing in finite elements was extended to the extended finite element method to form the smoothed extended finite element method (cell-based smoothed XFEM, edge-based smoothed XFEM, and node-based smoothed XFEM) [30–32]. By transforming interior integration into boundary integration, strain smoothing simplifies the integration of discontinuous approximations of the XFEM and suppresses the need to integrate singular functions numerically. The smoothed XFEM is insensitive to mesh distortion and locking and could be a competitive alternative to solve complex 3D problems. The strain smoothing method was extended to higher-order elements by [33], and it also concluded that the method is only beneficial when the enrichment functions are polynomial. Besides the XFEM, there are also some alternate approaches for modelling the strong discontinuity. The numerical results of the embedded finite element method (EFEM) and XFEM were compared in [34], and various methods for numerical modelling of multifield fracturing, such as interface and embedded discontinuity elements, XFEM, thick level set and phase field models, and a discrete crack approach with adaptive remeshing, were discussed in [35]. Recently, the meshfree method based on a partition of unity concept was also developed to model concrete and more general non-linear materials [36–38]. This method has been used to successfully model the reinforced concrete structural members at the ambient temperature [39,40], where a coupled particle-finite element approach was adopted and the reinforcement was coupled with the concrete via a 'barscale' bond model for modelling the pullout and splitting failure. However, so far, limited efforts have been made to use the XFEM in modelling reinforced concrete structural members in fire.

The main objective of this paper is to develop a robust finite element procedure for modelling the localised fracture of reinforced concrete members in fire conditions. The model developed can be used for structural fire engineering design of reinforced concrete beams and enable engineers to assess both the structural stability (global response) and the integrity (localised fracture) of the beams. In the past, the majority of reinforced concrete beams at elevated temperatures have been simulated by the conventional finite element method, in which the generalised isoparametric elements have usually been used. In the procedure proposed in this paper the isoparametric elements are still employed so that relatively small modifications of the available finite element model are required. The new procedure could be easily applied to the fire design for practical building structures. In this paper a 2D model is used to model reinforced concrete beams. Since mesh distortion and locking are not the main concerns within the scope of this paper, only the straight crack is considered and the standard XFEM formulations and numerical integration procedure are employed. In this new model a reinforced concrete beam is represented as an assembly of 4-node quadrilateral plain concrete, 3-node main reinforcing steel bar, and 2-node bond-link elements. The extended finite element method (XFEM) is incorporated into plain concrete elements in order to capture the localised cracks of concrete within the member. The original contributions of the model presented in this paper are:

- Combine the XFEM plain concrete element with the reinforcing bar element and bond-link element successfully. Due to the bond-link element and plain concrete element sharing the same node, one important issue with which the model should deal is the compatibility of nodal displacements referenced to the plain concrete element and bond-link element. This is due to the nodal displacement of the cracked XFEM plain concrete element being divided into two parts: continuous part and discontinuous part. These displacements are not compatible with the nodal displacement of the bond-link element. Therefore, a special shifted enhancement function is used in order to obtain the total nodal displacement (including both continuous and discontinuous parts) of the cracked XFEM plain concrete elements. This satisfies the compatibility of the nodal displacements of both the XFEM plain concrete element and bond-link element.
- With the help of the bond-link element and steel bar element, the developed model has the capability to consider the influence of the bond characteristic between the concrete and reinforcing steel bar on the initiation and propagation of each individual crack within the reinforced concrete beam. Due to the influence of the reinforcing steel bar, the Newton–Raphson iteration procedure can be employed to solve this very nonlinear problem up to the failure of the whole beam. This is significantly different with conventional XFEM models, in which a complex solution procedure needs to be developed.
- Even for the adoption of a 2D model for modelling plain concrete, the model developed in this paper is still complex, because the effects of temperatures induced by fire need to be taken into account. The XFEM plain concrete elements are subdivided into layers for considering the temperature distribution over the cross-section of a beam. Since the temperature varies across different layers, a robust criterion has been developed to determine the initiation of individual cracks within the XFEM plain concrete elements. Moreover, the complications of structural behaviour in fire, such as thermal expansion, degradation of bond characteristics between a reinforcing steel bar and concrete, and the change of material properties with temperature, are modelled.

The new model has been validated against some previous fire tests of reinforced concrete beams. It is clear that the developed nonlinear procedure proposed in this paper can predict cracking patterns (flexural cracks and shear cracks) of the reinforced concrete beams properly. The model is capable of predicting the global response of reinforced concrete beams in fire with good

accuracy and, at the same time, capturing the formation and propagation of individual localised cracks within the beams. The influences of bond characteristics between the concrete and reinforcing steel bar on the deflection and crack opening are also examined in this paper. The model presented in this paper provides a very useful tool for researchers and designers to assess the integrity of reinforced concrete structural members under fire conditions.

2. Development of the nonlinear procedure

As shown in Fig. 1, a reinforced concrete beam is modelled as an assembly of plain concrete, main reinforcing steel bar, and bond-link elements. The plain concrete elements are subdivided into layers to take into account the temperature distribution over the cross-section of a beam. The bond-link elements are used to represent the interaction between the plain concrete and reinforcing steel bar elements.

2.1. Layered quadrilateral concrete elements with extended finite element formulations

Fig. 2 shows a 4-node layered quadrilateral element to simulate the plain concrete for a reinforced concrete beam under fire conditions. Each node of the element contains two translational degrees of freedom. In order to consider the temperature distribution over the beam cross-section, the plain concrete elements are divided into layers in the z direction, and each layer can have a different but uniform temperature. The initial material properties of each layer may be different. Concrete layers are in a state of plane stress, so the material property, temperature, load and deformation of the element are symmetric to the reference plane (mid-plane, as shown in Fig. 2) along the thickness [41]. Within the element the stress–strain relationships may change independently for each layer. Since temperature-dependent constitutive models are used in this study, the material properties and thermal expansions vary at different layers, but are constant within a layer at each temperature step.

2.1.1. Element stiffness matrix, K

In order to model the localised fracture of plain concrete, the extended finite element method (XFEM) is used for the development of plain concrete elements. The model proposed here can capture individual concrete cracks without remeshing and calculating the magnitude of individual crack openings during the analysis. The key idea of the extended finite element method (XFEM) is to use the partition of unity for describing the discontinuous displacement, and then the displacement field is approximated by the sum of the regular displacement and the enhancement displacement fields [16]. In order to do this, extra degrees of freedom are added on the enhanced nodes to represent the enhancement displacement field. Special enhancement functions are also employed to realise the displacement jump over the discontinuity. Note that many applications of the XFEM have been conducted using a step function to enrich the element which is completely cut by a crack and using branch functions to enrich the element which the crack tip located inside the element. In this paper, for simplicity, it is assumed that the crack tip is always located on an edge of an element; thus, the cracked element can be successfully enriched by the *sign* function only without other enrichment functions. Thus, the crack branching is not included in the proposed procedure, assuming that a particular element

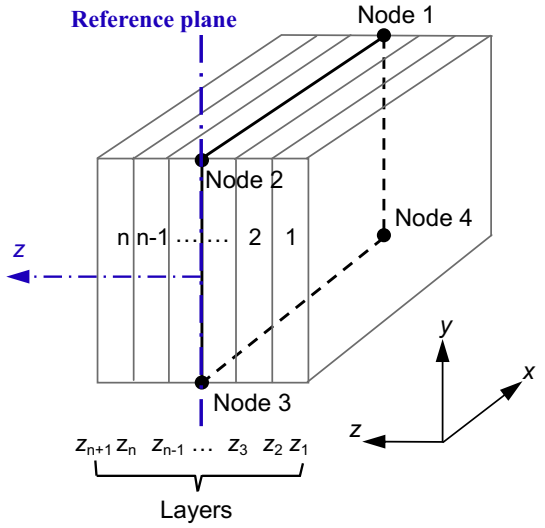

Fig. 2. A layered 4-node quadrilateral plain concrete element.

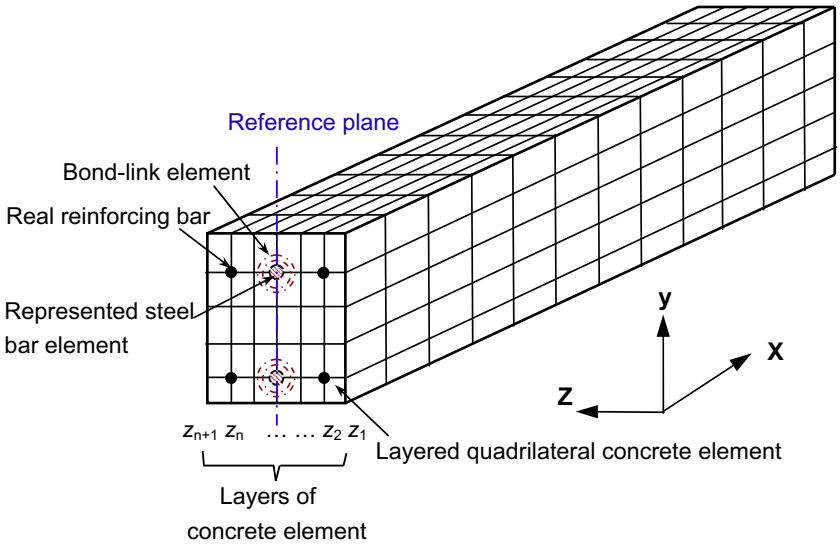

Fig. 1. Nonlinear layered finite element procedure for modelling a reinforced concrete beam.

contains one crack only. The main purpose of the model developed in this paper is to predict the global response of reinforced concrete beams in fire with reasonable accuracy and, at the same time, the major localised cracks within the beam can also be captured. Therefore, in order to enhance the computational efficiency of the proposed model, precise modelling of the crack tip and crack branching is not considered in this paper.

Considering a four-node quadrilateral element crossed by a discontinuity (Γ_d) (see Fig. 3), the domain is divided into two distinct domains referenced to an element, which are represented as Ω^+ and Ω^- on the different sides of the discontinuity in an element. Figs. 3(a) and (b) give the definition of sub-domains Ω^+ and Ω^- where a discontinuity cuts a quadrilateral element in two different possible ways, respectively. Then, the total displacement field **u**consists of a continuous regular displacement field $\mathbf{u}_{cont}$ and a discontinuous displacement field $\mathbf{u}_{dis}$[18], that is:

$$\mathbf{u} = \mathbf{u}_{\text{cont}} + \mathbf{u}_{\text{dis}} = \sum_{1}^{4} N_i \mathbf{u}_i + \sum_{1}^{4} N_i \Psi_i(\mathbf{x}) \mathbf{a}_i \tag{1}$$

where N_i is the shape function, $\mathbf{u}_i$ is the regular node displacement, $\mathbf{a}_i$ is the additional node displacement to describe the discontinuity, and $\Psi_i(\mathbf{x})$ is the enhancement function:

$$\Psi_i(\mathbf{x}) = sign(x) - sign(x_i) \qquad (i = 1 \sim 4) \tag{2}$$

in which *sign* is the sign function and defined as:

$$sign(x) = \begin{cases} +1 & \text{if } x \in \Omega^+ \\ -1 & \text{if } x \in \Omega^- \end{cases} \tag{3}$$

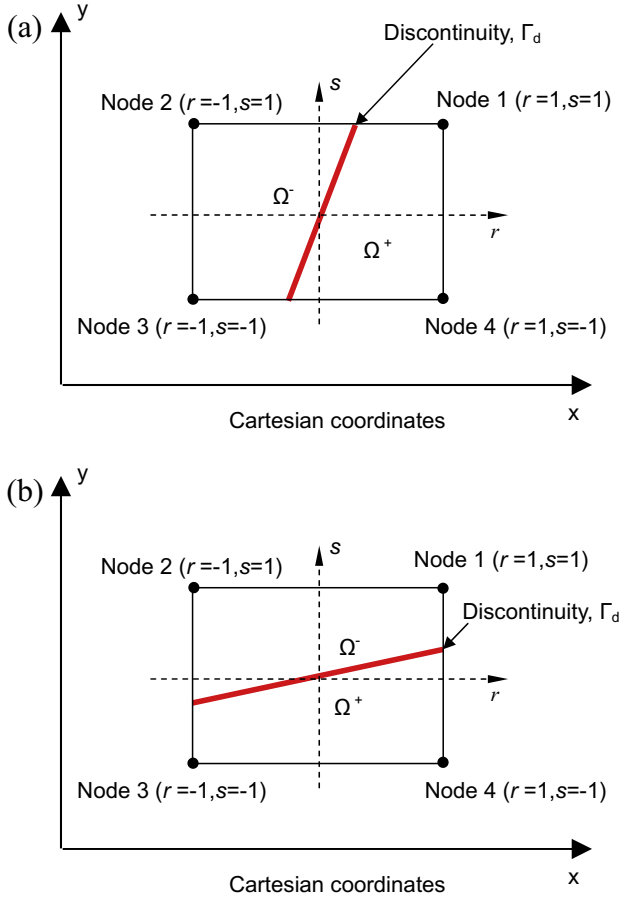

Fig. 3. A 4-node quadrilateral element crossed by a discontinuity Γ_d.

Note that the *sign* function enrichment is equivalent to the Heaviside step function enrichment which has been used in many previous XFEM models. But the *sign* function appears more symmetrical [19]. $sign(x_i)$ is the value of the *sign* function of the *i-th* node in a quadrilateral element. Taking the quadrilateral element in Fig. 3(a) as an example: $sign(x_2) = sign(x_3) = -1$ for nodes 2 and 3 and $sign(x_1) = sign(x_4) = +1$ for nodes 1 and 4, respectively. Compared with the conventional XFEM models, the *sign* function given in Eq. (2) is shifted by $sign(x_i)$. According to [19], using the shifted *sign* function can make the enrichment displacement field vanish outside the enhanced element.

One significant advantage of using the *sign* function is that only the elements cut by the crack need to be enhanced, as the resulting enhancement vanishes in all elements not crossed by the crack. The utilisation of a shifted *sign* function may greatly simplify the implementation of the extended finite element model, without altering the approximating basis. Especially for modelling reinforced concrete structures, this advantage is more significant because multiple cracks normally are distributed within a reinforced concrete member (due to the bond action between steel bars and concrete). Other than the simplification in terms of implementing the procedure, the key reason for using the shifted enhancement function is to obtain the total nodal displacement directly from the procedure, rather than only the regular part of XFEM nodal displacement being outputted from the procedure [42]. This makes the compatibility of total nodal displacements of the plain concrete element and bond-link element feasible. Therefore, the bond-link element can be used to link plain concrete elements and steel bar elements in a conventional way, such as through the continuous approach, for modelling localised cracking within a reinforced concrete member.

In the case of the four-node quadrilateral element (Fig. 3), the element nodal displacement vector $\hat{\mathbf{u}}$ can be represented as:

$$\hat{\mathbf{u}} = \begin{Bmatrix} \mathbf{u}_i \\ \mathbf{a}_i \end{Bmatrix} = [u_1 \;\; v_1 \;\; u_2 \;\; v_2 \;\; u_3 \;\; v_3 \;\; u_4 \;\; v_4 \;\; a_1 \;\; b_1 \;\; a_2 \;\; b_2 \;\; a_3 \;\; b_3 \;\; a_4 \;\; b_4]^T \tag{4}$$

where u_i and v_i are the regular nodal displacements related to x and y coordinates, respectively, and a_i and b_i are the enhanced nodal displacements related to x and y coordinates, respectively.

Thus, the strains ($\boldsymbol{\varepsilon}$) within an enhanced element consist of the regular and enhancement parts, which are related to the regular nodal and enhanced nodal displacements respectively. The strain vector $\boldsymbol{\varepsilon}$ can be expressed as:

$$\boldsymbol{\varepsilon} = \boldsymbol{\varepsilon}_{cont} + \boldsymbol{\varepsilon}_{dis} = \begin{Bmatrix} \varepsilon_x \\ \varepsilon_y \\ \gamma_{xy} \end{Bmatrix} = \mathbf{B}\hat{\mathbf{u}} = \begin{bmatrix} \mathbf{B}^u_{sta} & \mathbf{B}^a_{enr} \end{bmatrix} \begin{Bmatrix} \mathbf{u}_i \\ \mathbf{a}_i \end{Bmatrix} \tag{5}$$

where $\boldsymbol{\varepsilon}_{cont}$ is the continuous strain, and $\boldsymbol{\varepsilon}_{dis}$ is the discontinuous strain. $\mathbf{B}^u_{sta}$ is the standard strain–displacement transformation matrix corresponding to the regular degrees of freedom $\mathbf{u}_i$, and $\mathbf{B}^a_{enr}$ is the enrichment strain–displacement transformation matrix corresponding to the additional degrees of freedom $\mathbf{a}_i$.

The strain–displacement transformation matrix **B** including the regular part and enhancement part can be obtained as $\mathbf{B} = [\mathbf{B}^u_{sta} \mathbf{B}^a_{enr}]$, in which:

$$\begin{aligned} \mathbf{B}^u_{sta} &= \mathbf{L}\mathbf{N} = \mathbf{L} \begin{bmatrix} N_1 & 0 & N_2 & 0 & N_3 & 0 & N_4 & 0 \\ 0 & N_1 & 0 & N_2 & 0 & N_3 & 0 & N_4 \end{bmatrix} \\ &= \begin{bmatrix} B_{sta1x} & 0 & B_{sta2x} & 0 & B_{sta3x} & 0 & B_{sta4x} & 0 \\ 0 & B_{sta1y} & 0 & B_{sta2y} & 0 & B_{sta3y} & 0 & B_{sta4y} \\ B_{sta1y} & B_{sta1x} & B_{sta2y} & B_{sta2x} & B_{sta3y} & B_{sta3x} & B_{sta4y} & B_{sta4x} \end{bmatrix} \end{aligned} \tag{6}$$

$$\mathbf{B}^a_{enr} = \Psi_i(\mathbf{x})\mathbf{L}\mathbf{N} = \mathbf{L}\begin{bmatrix} \Psi_1(x)N_1 & 0 & \Psi_2(x)N_2 & 0 & \Psi_3(x)N_3 & 0 & \Psi_4(x)N_4 & 0 \\ 0 & \Psi_1(x)N_1 & 0 & \Psi_2(x)N_2 & 0 & \Psi_3(x)N_3 & 0 & \Psi_4(x)N_4 \end{bmatrix}$$
$$= \begin{bmatrix} B_{enr1x} & 0 & B_{enr2x} & 0 & B_{enr3x} & 0 & B_{enr4x} & 0 \\ 0 & B_{enr1y} & 0 & B_{enr2y} & 0 & B_{enr3y} & 0 & B_{enr4y} \\ B_{enr1y} & B_{enr1x} & B_{enr2y} & B_{enr2x} & B_{enr3y} & B_{enr1x} & B_{enr4y} & B_{enr4x} \end{bmatrix} \tag{7}$$

where $\mathbf{N}$ is the shape function of a general quadrilateral element [43], $\Psi_i(\mathbf{x})(i = 1–4)$ is the enrichment function given in Eq. (2), and the matrix $\mathbf{L}$ contains differential operators.

Since the effect of thermal expansion is included in the model, the total strains ($\boldsymbol{\varepsilon}$) include both thermal and stress-related strains at elevated temperatures. The stress-related strains can be obtained by deducing the thermal strains ($\boldsymbol{\varepsilon}_T$) from the total strains ($\boldsymbol{\varepsilon}$). If strains are reasonably small the stress vector $\boldsymbol{\sigma}$ can be obtained from the stress-related strain vector as:

$$\boldsymbol{\sigma} = \begin{Bmatrix} \sigma_x \\ \sigma_y \\ \tau_{xy} \end{Bmatrix} = \mathbf{D}(\boldsymbol{\varepsilon} - \boldsymbol{\varepsilon}_T) = \mathbf{D}\left(\mathbf{B}^u_{sta}\mathbf{u}_i + \Psi_i(\mathbf{x})\mathbf{B}^u_{sta}\mathbf{a}_i - \boldsymbol{\varepsilon}_T\right) \tag{8}$$

in which $\mathbf{D}$ is the constitutive matrix of concrete related to plane stress.

In a finite element model, the equilibrium conditions between internal and external 'forces' have to be satisfied. To form the element stiffness matrix and internal force vector, the virtual work equation without body force reads as:

$$\mathbf{f}^{int} = \int_\Omega \mathbf{B}^{\mathrm{T}}\boldsymbol{\sigma}\, d\Omega = \mathbf{f}^{\mathrm{ext}} \tag{9}$$

where $\mathbf{f}^{int}$ is the internal force vector, and $\mathbf{f}^{\mathrm{ext}}$ is the external force vector. In this study the cracked concrete is treated as a quasi-brittle heterogeneous material, and the cohesive crack concept is used for simulating quasi-brittle fracture. The internal force vector $\mathbf{f}^{int}$ contains the regular part ($\mathbf{f}^{int}_u$), the enhancement part ($\mathbf{f}^{int}_a$), and the traction part ($\mathbf{f}^{int}_\Gamma$). The regular internal force ($\mathbf{f}^{int}_u$) balances the external force ($\mathbf{f}^{\mathrm{ext}}$), and the enhancement part ($\mathbf{f}^{int}_a$) is related to the traction of the crack ($\mathbf{f}^{int}_\Gamma$) only [18], that is:

$$\mathbf{f}^{int}_u = \int_\Omega \mathbf{B}^{u^T}_{sta}\boldsymbol{\sigma}\, d\Omega = \mathbf{f}^{\mathrm{ext}} \tag{10}$$

$$\mathbf{f}^{int}_a + \mathbf{f}^{int}_\Gamma = \int_{\Omega^+,\Omega^-} \mathbf{B}^{a^T}_{enr}\boldsymbol{\sigma}\, d\Omega + \int_{\Gamma_d} \overline{\mathbf{N}}^T\mathbf{t}_a\, d\Gamma_d = 0 \tag{11}$$

where $\mathbf{t}_a$ is the traction acting on the discontinuity and can be written as:

$$\mathbf{t}_a = \begin{Bmatrix} t_{an} \\ t_{as} \end{Bmatrix} = \mathbf{T}_a\mathbf{w} = \begin{bmatrix} T_{an} & 0 \\ 0 & 0 \end{bmatrix}\begin{Bmatrix} w_n \\ w_s \end{Bmatrix} \tag{12}$$

where t_{an} and t_{as} are the traction normal and tangential to a crack, respectively; w_n and w_s are the crack opening normal and tangential to a crack, respectively; and T_{an} is the tangent stiffness of the traction–separation law.

In order to solve the nonlinear problem, an incremental solution procedure needs to be developed. By substituting the rate form of the constitutive relations of Eq. (8) into Eqs. (10) and (11), the element stiffness matrix in terms of incremental displacements can be obtained as:

$$\mathbf{K}\,\dot{\mathbf{d}}\mathbf{u} = \begin{bmatrix} \mathbf{K}_{uu} & \mathbf{K}_{ua} \\ \mathbf{K}_{au} & (\mathbf{K}_{aa} + \mathbf{K}_\Gamma) \end{bmatrix}\begin{Bmatrix} \mathbf{du}_i \\ \mathbf{da}_i \end{Bmatrix} = \begin{Bmatrix} \mathbf{f}^{\mathrm{ext}} \\ 0 \end{Bmatrix} - \begin{Bmatrix} \mathbf{f}^{int}_u \\ \mathbf{f}^{int}_a + \mathbf{f}^{int}_\Gamma \end{Bmatrix} \tag{13}$$

where $\mathbf{K}_{uu}$ is the element stiffness matrix referenced to the regular degrees of freedom, $\mathbf{K}_{aa}$ is the element stiffness matrix related to the enhancement degrees of freedom, $\mathbf{K}_{ua} = \mathbf{K}^T_{au}$ is related to both, and $\mathbf{K}_\Gamma$ is the element stiffness matrix related to traction. They are expressed as:

$$\mathbf{K}_{uu} = \int_\Omega \mathbf{B}^{u^T}_{sta}\mathbf{D}\mathbf{B}^u_{sta}\, d\Omega = \iint_A \mathbf{B}^{u^T}_{sta}\left(\int \mathbf{D}_l dz\right)\mathbf{B}^u_{sta}\, dx\, dy \tag{14}$$

$$\mathbf{K}_{ua} = \int_{\Omega^+,\Omega^-} \mathbf{B}^{u^T}_{sta}\mathbf{D}\mathbf{B}^a_{enr}\, d\Omega = \iint_{A^+,A^-} \mathbf{B}^{u^T}_{sta}\left(\int \mathbf{D}_l dz\right)\mathbf{B}^a_{enr}\, dx\, dy \tag{15}$$

$$\mathbf{K}_{au} = \int_{\Omega^+,\Omega^-} \mathbf{B}^{a^T}_{enr}\mathbf{D}\,\mathbf{B}^u_{sta}\, d\Omega = \iint_{A^+,A^-} \mathbf{B}^{a^T}_{enr}\left(\int \mathbf{D}_l dz\right)\mathbf{B}^u_{sta}\, dx\, dy \tag{16}$$

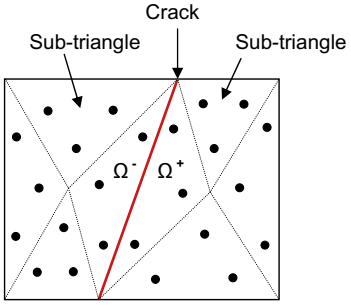

(a) A crack cutting a concrete element into two quadrilaterals

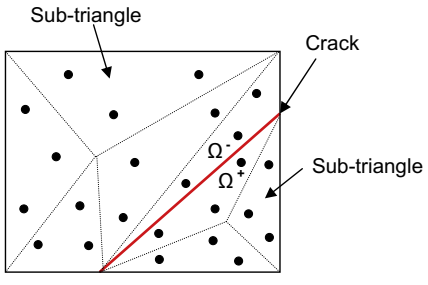

(b) A crack cutting a concrete element into a pentagon and a triangle

Fig. 4. Integration scheme for an enhanced 4-node quadrilateral element crossed by a crack.

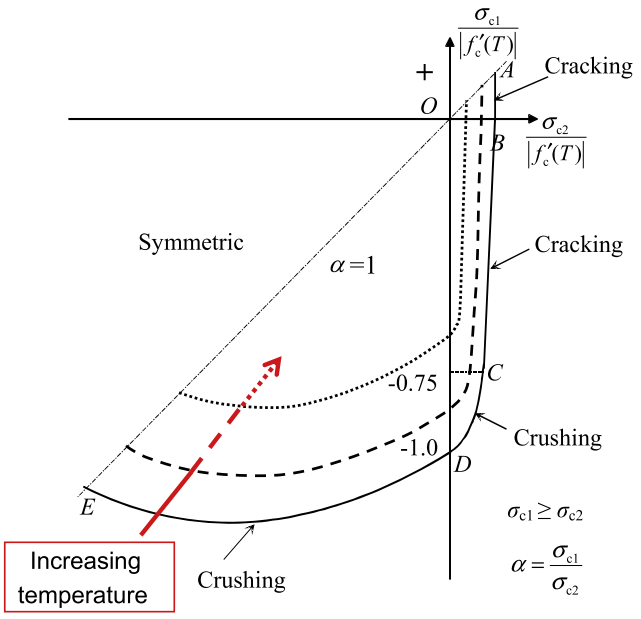

Fig. 5. Concrete biaxial failure envelopes at elevated temperatures.

$$\mathbf{K}_{aa} = \int_{\Omega^+,\Omega^-} \mathbf{B}_{enr}^{a^T}\, \mathbf{D}\mathbf{B}_{enr}^{a}\, d\Omega = \iint_{A^+,A^-} \mathbf{B}_{enr}^{a^T} \left(\int \mathbf{D}_l dz \right) \mathbf{B}_{enr}^{a}\, dx\, dy \quad (17)$$

$$\mathbf{K}_{\Gamma} = \int_{\Gamma_d} \overline{\mathbf{N}}^{\mathbf{T}} \mathbf{T}_{\mathbf{a}} \overline{\mathbf{N}} \mathbf{d} \Gamma_{\mathbf{d}} = \int_{\Gamma_d} \overline{\mathbf{N}}^{\mathbf{T}} \mathbf{O}^{\mathbf{T}} \mathbf{T}_{\mathbf{d}} \mathbf{O} \overline{\mathbf{N}} \mathbf{d} \Gamma_{\mathbf{d}}$$
$$= \int_{\Gamma_d} \overline{\mathbf{N}}^{T} \mathbf{O}^{T} \left(\int \mathbf{T}_{dl}\, dz \right) \mathbf{O} \overline{\mathbf{N}}\, d\Gamma_d \quad (18)$$

where $\overline{\mathbf{N}} = 2(\mathbf{N})$ and $\mathbf{N}$ is the shape function, $\mathbf{T}_d$ is the tangent stiffness of the traction–separation law, and $\mathbf{O}$ is the orthogonal transformation matrix – for the transformation of the local orientation of the discontinuity to the global coordinate system. The expression of $\mathbf{O}$ can be found in [44].

In this study, Gauss quadrature is employed to calculate the stiffness matrix of quadrilateral elements. Therefore, all stresses, strains, and the constitutive matrix of material discussed above correspond to Gauss integration points. Since the elements are divided into layers along the z- axis (see Fig. 2), and the material properties are assumed to be constant within each layer at each time or temperature step, the matrices $\mathbf{D}$ and $\mathbf{T}_d$ in Eqs. (14)–(18) at a Gauss point are a function of $z$only, and the inner integrations $(\int \mathbf{D}_l dz)$ and $(\int \mathbf{T}_{dl} dz)$ can be performed separately. Integration along the z- axis is replaced by summation over the layers as:

$$\int \mathbf{D}_l dz = \sum_{l=1}^{n} (z_{l+1} - z_l) \mathbf{D}_l \quad (19)$$

$$\int \mathbf{T}_{dl} dz = \sum_{l=1}^{n} (z_{l+1} - z_l) \mathbf{T}_{dl} \quad (20)$$

where

z_l is the distance from the reference plane to the l-th layer (Fig. 2),
$\mathbf{D}_l$ is the material stiffness matrix for the l-th layer,
$\mathbf{T}_{dl}$ is the tangent stiffness matrix of traction–separation law for the l-th layer, and
n is the total number of element layers.

2.1.2. Element internal force vector, f^{int}

Using the principle of virtual work, the internal force vectors can be written as [18]:

$$\mathbf{f}_u^{int} = \int_{\Omega} \mathbf{B}_{sta}^{u^T}\, \boldsymbol{\sigma}\, d\Omega = \iint_{A} \mathbf{B}_{sta}^{u^T} \left(\int \boldsymbol{\sigma}_l dz \right) dx\, dy \quad (21)$$

$$\mathbf{f}_a^{int} = \int_{\Omega^+,\Omega^-} \mathbf{B}_{enr}^{a^T}\, \boldsymbol{\sigma}\, d\Omega = \iint_{A^+,A^-} \mathbf{B}_{enr}^{a^T} \left(\int \boldsymbol{\sigma}_l dz \right) dx\, dy \quad (22)$$

$$\mathbf{f}_{\Gamma}^{int} = \int_{\Gamma_d} \overline{\mathbf{N}}^{T} \mathbf{t}_a\, d\Gamma_d = \int_{\Gamma_d} \overline{\mathbf{N}}^{T} \mathbf{O}^{T} \left(\int \mathbf{t}_{dl}\, dz \right) d\Gamma_d \quad (23)$$

As mentioned above, the Gauss quadrature is used to calculate $\mathbf{f}_u^{int}$, $\mathbf{f}_a^{int}$ and $\mathbf{f}_{\Gamma}^{int}$. Therefore, $(\int \boldsymbol{\sigma} dz)$ and $(\int \mathbf{t}_{dl} dz)$ at a Gauss point are a function of z only, and the inner integrations $\int \boldsymbol{\sigma}_l dz$ and $\int \mathbf{t}_{dl} dz$ in Eqs. (21)–(23) can be expressed by summation over the layers as:

$$\int \boldsymbol{\sigma}_l dz = \sum_{l=1}^{n} (z_{l+1} - z_l) \boldsymbol{\sigma}_l \quad (24)$$

$$\int \mathbf{t}_{dl} dz = \sum_{l=1}^{n} (z_{l+1} - z_l) \mathbf{t}_{dl} \quad (25)$$

where $\boldsymbol{\sigma}_l$ is the stress vector in the l-th layer, $\mathbf{t}_{dl}$ is the traction in the l-th layer, and n is the total number of layers.

In this study, Gauss quadrature is employed to calculate the stiffness matrix and internal force vector of the concrete element. $\mathbf{K}_{uu}$ and $\mathbf{f}_u^{int}$ can be integrated in the usual way over the whole domain (Ω), but for $\mathbf{K}_{aa}$, $\mathbf{K}_{ua}$, $\mathbf{K}_{au}$ and $\mathbf{f}_a^{int}$, integration should be performed separately on both sides (Ω^+ and Ω^-) of the crack, respectively. This means that the *sign* function *sign* (x) needed to be applied for each Gauss point within the element. In the current model, a crack is represented by a straight line within the enhancement element, with two Gauss points employed to integrate the discontinuity terms $\mathbf{K}_{\Gamma}$ and $\mathbf{f}_{\Gamma}^{int}$ over the discontinuity Γ_d using a one-dimensional integration scheme. For the regular four-node element without a crack, four Gauss integration points are used (as recommended by Bathe [43]). But for those enhanced elements containing a crack, conventional four Gauss integration is insufficient to distinguish the enhancement function from a constant function over different sides (Ω^+ and Ω^-) of the crack, resulting in linearly independent shape functions [18]. Therefore, the enhanced elements need to be integrated separately on each side

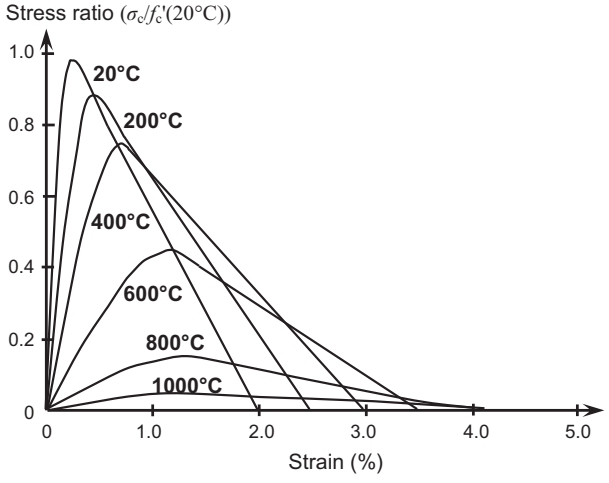

Fig. 6. Uniaxial compressive stress–strain relationships of concrete at elevated temperatures.

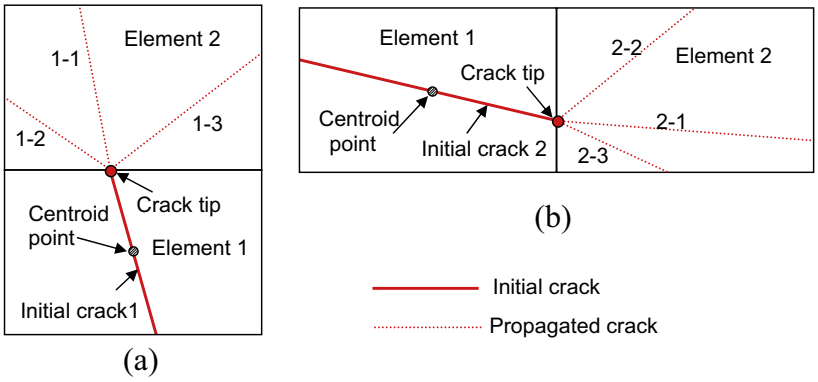

Fig. 7. Crack initiation and propagation.

of the crack. Note that there are many different integration schemes that could be used for an enhanced quadrilateral element with sufficient accuracy [45]. In this paper the scheme that partitioned the element into sub-triangles is adopted for its flexibility because it might be desirable to add other enhancement functions into the procedure in future research. Then, in the case of the element being cut by a crack into two sub-quadrilaterals, as shown in Fig. 4(a), four sub-triangles with 12 Gauss points are applied within each sub-quadrilateral. Fig. 4(b) shows the element being cut by a crack into a pentagon and a triangle. In this case, five sub-triangles with 15 Gauss points are applied within the pentagon, and three sub-triangles with nine Gauss points are used within the triangle. More detailed information related to the integration schemes can be found in [44]. Due to the high non-linearity of the current model, a full Newton–Raphson solution procedure is adopted.

2.1.3. Constitutive modelling of concrete at elevated temperatures

Before cracking or crushing occurs, the concrete is assumed to be isotropic, homogeneous, and linearly elastic. Barzegar-Jamshidi [46] proposed a biaxial concrete failure envelope at an ambient temperature, which was based on a slight modification of the Kupfer and Gerstle [47] expressions. At present, there are still very little data and few theoretical models available regarding the constitutive modelling of concrete under biaxial states of stress at elevated temperatures. Based on the Barzegar-Jamshidi [46] model, Huang et al. [11] developed a biaxial concrete failure envelope at elevated temperatures by considering all of the relevant material properties as temperature-dependent. As shown in Fig. 5, with the increasing temperatures the area enclosed by the failure envelope tends to be decreasing. The model was validated against the test results in [11,12]. Therefore, this model is adopted to determine the cracking and crushing of concrete in this paper. In the figure, $f_c'(T)$ and $f_t'(T)$ are the temperature-dependent compressive strength and tensile strength of concrete, respectively; σ_{c1} and σ_{c2} are the principal stresses. The failure surfaces of the biaxial strength envelope are divided into four regions which depend on the stress state as represented by the principal stress ratio $\alpha = \sigma_{c1}/\sigma_{c2}$. It is assumed that compressive stresses are negative and tensile stresses are positive, and the principal directions are chosen so that $\sigma_{c1} \geqslant \sigma_{c2}$ algebraically.

The four regions of the failure surfaces of the strength envelope in Fig. 5 can be expressed as follows:

(1) In the tension–tension region ($\sigma_{c1} = tension$, $\sigma_{c2} = tension$), line segment A–B, failure by cracking:

$$\left.\begin{aligned}\sigma_{c1} &= f_t' \\ \sigma_{c2} &= \frac{\sigma_{c1}}{\alpha}\end{aligned}\right\} \quad \alpha \geqslant 1.0$$

(2) In the tension–compression region ($\sigma_{c1} = tension$, $\sigma_{c2} = compression$), line segment B–C, failure by cracking:

$$\left.\begin{aligned}\sigma_{c1} &= \alpha\sigma_{c2} \\ \sigma_{c2} &= \frac{f_t'}{\alpha - 0.6r}\end{aligned}\right\} \quad \alpha \leqslant -0.73r$$

where $r = f_t'/|f_c'|$.

(3) In the tension–compression region ($\sigma_{c1} = tension$, $\sigma_{c2} = compression$), line segment C–D, failure by crushing:

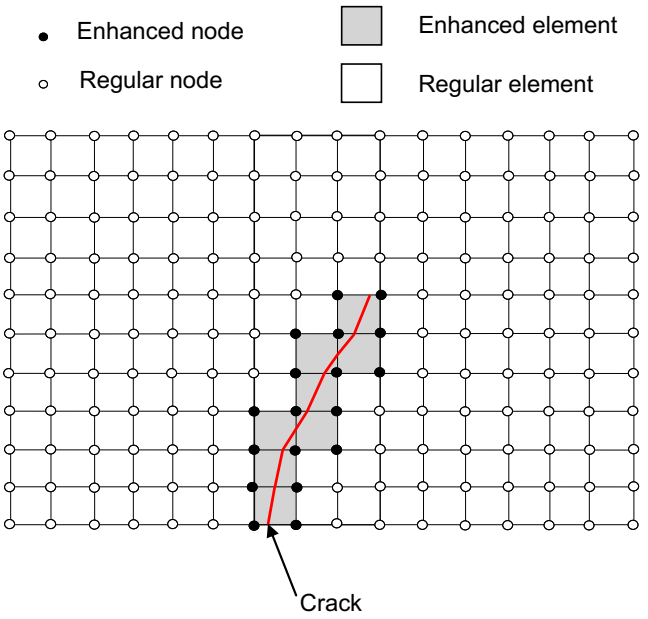

Fig. 8. The finite element mesh for a plain concrete structure with a crossed crack.

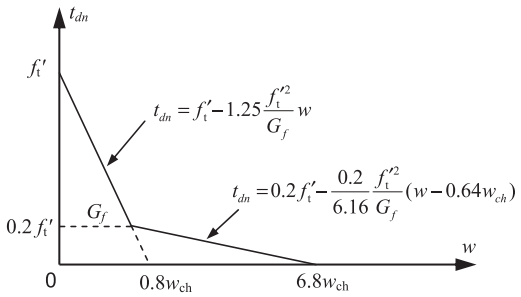

Fig. 9. Bi-lineal softening fracture curve of concrete.

$$\left.\begin{aligned}\sigma_{c1} &= \alpha\sigma_{c2}\\ \sigma_{c2} &= \frac{f'_c}{12.8r}\left[9r+\alpha+\sqrt{(9r+\alpha)^2-66.56r^2}\right]\end{aligned}\right\} \quad -0.73r<\alpha\leqslant 0$$

(4) In the compression–compression region (σ_{c1} = *compression*, σ_{c2} = *compression*), line segment D–E, failure by crushing:

$$\left.\begin{aligned}\sigma_{c1} &= \alpha\sigma_{c2}\\ \sigma_{c2} &= \frac{1+3.65\alpha}{(1+\alpha)^2}f'_c\end{aligned}\right\} \quad 0<\alpha\leqslant 1$$

Within this model the initiation of a cracking or crushing process at any location occurs when the concrete stresses reach one of the failure surfaces. It is also assumed that after concrete crushing, all strength and stiffness are lost. The main advantages of this model are that it is simple and the required data are readily obtainable from uniaxial tests on the concrete.

As shown in Fig. 6, the models specified in EN1992-1-2 [48] are adopted to determinate the uniaxial properties of concrete at elevated temperatures. The uniaxial tensile strength of concrete (in MPa) is obtained by $f'_t(T)=0.3321\sqrt{f'_c(T)}$ [49]. Therefore, the concrete tensile strength $f'_t(T)$ changes with temperature as well. The thermal elongation of concrete is calculated according to the model suggested by EN1992-1-2 [48]. For concrete in the biaxial stresses case, it is assumed that free thermal expansion produces zero shear strain.

2.1.4. The determination of enhancement elements and nodes

Under fire conditions, each concrete layer within an element has different temperatures and material properties. The magnitude and orientation of principle stresses at a Gauss point may also not be the same for each layer. Therefore, the failure envelope of concrete at a Gauss point, which is temperature-dependent, may change over the different concrete layers. Thus, a criterion is needed for determining whether or not an element should be enhanced. In this study, the weighted average values of maximum principal stresses and concrete material properties over the element are proposed to examine the initiation of cracks in an element. For an element the weighted average stress in the x direction ($\sigma_{x,ave}$) and the weighted average tensile strength of concrete $f_{t,ave}(T)$ can be expressed as (see Fig. 2):

$$\sigma_{x,ave}=\frac{\sum_{l=1}^{n}\sum_{g=1}^{m}\sigma^l_{x,g}(z_{l+1}-z_l)}{m(z_{n+1}-z_1)} \tag{26}$$

$$f_{t,ave}(T)=\frac{\sum_{l=1}^{n}f^l_t(T)(z_{l+1}-z_l)}{z_{n+1}-z_1} \tag{27}$$

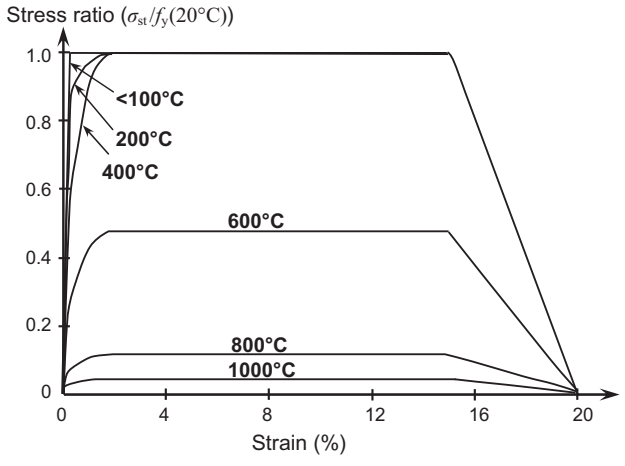

Fig. 10. Stress–strain relationships of reinforcing steel at elevated temperatures.

where

$\sigma_{x,ave}$ is the average stress in the x direction,
$f_{t,ave}(T)$ is the average tensile strength of concrete,
$\sigma^l_{x,g}$ is the stress in the x direction at the g-th Gauss point of the l-th layer,
$f^l_t(T)$ is the tensile strength of the l-th layer concrete,
m is the total number of Gauss points in each layer,
n is the total layer number of an element, and
$(z_{n+1}-z_1)$ is the total thickness of an element.

Using the same procedure, the weighted average stress in the y direction ($\sigma_{y,ave}$) and the weighted average shear stress ($\sigma_{xy,ave}$) can also be calculated. The weighted average principle stresses $\sigma_{p1,ave}$ and $\sigma_{p2,ave}$ can be obtained from $\sigma_{x,ave}, \sigma_{y,ave}$ and $\sigma_{xy,ave}$. Again, the same method is used to calculate the weighted average compressive strength $f'_{c,ave}(T)$, and weighted average modulus of elasticity $E_{c,ave}(T)$, for the concrete element. Based on those parameters the biaxial concrete failure envelope (see Fig. 5) can be constructed for each concrete element at each time or temperature step.

At each time or temperature increment, all concrete elements are examined one by one. Once the average principal tensile stresses of a concrete element reach one of the 'average failure surfaces', either in the biaxial tension region or in the combined tension–compression region, a straight crack is inserted through the entire element, and the orientation of the crack is normal to the average maximum tensile principal stress. The initial crack is assumed to go through the centroid point of a quadrilateral element. Then, when the average principal stresses of the next element reach one of the tension failure surfaces, the crack will propagate from the tip of the existing crack into the next element, following the orientation normal to the corresponding average maximum tensile principal stress of the element. Fig. 7 illustrates how a crack initiates and propagates. As can be seen, there are two different possible ways in which an initial crack cuts a quadrilateral element: initial crack 1 in Fig. 7(a) and initial crack 2 in Fig. 7(b), each of which has possibly three crack propagation paths within the next element when the initial crack extends from element 1 into element 2.

Since the enhancement function (*sign* function) related to enhancement nodes is shifted by *sign* (x_i), the enhanced displacement field vanishes outside the element enclosing the crack. Thus, only the elements crossed by the crack need to be enhanced, rather than all of the elements that contain enhanced nodes. This

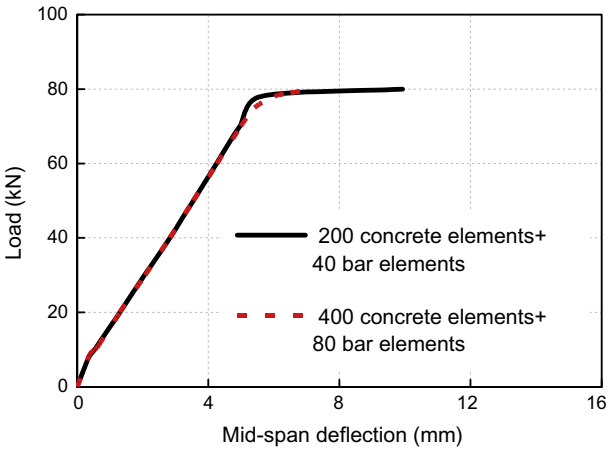

Fig. 11. Comparison of predicted loads versus mid-span deflection curve using different FE meshes.

procedure is illustrated in Fig. 8, where the enhanced elements are filled with grey colour, and the enhanced nodes are indicated by the solid circles and regular nodes by the hollow circles. To model multiple cracks within a reinforced concrete member, the model developed in this paper allows two or more cracks to initiate and propagate at the same time. For simplicity, it is assumed that only one crack may exist within a particular element.

After concrete cracking, the constitutive model based on the cohesive crack concept [50] is adopted for the cracked concrete element. The crack opening is related to the traction forces acting on the crack. The constitutive model is formed in an orthogonal local coordinate system (n,t) related to the crack, in which the n direction is normal to the crack and the t direction is tangential to the crack. Note that in the cohesive cracks, although the crack faces are not in contact the frictional forces may still exist between the faces due to the applied cohesive stresses if there is relative sliding [51]. However, for the reinforced concrete beam modelled in this paper, the friction between crack faces will not play an important role in the structural behaviour of the beam, due to the fact that the beam is mainly dominated by bending rather than shear. Therefore, the friction between cohesive crack faces was ignored in the current model. The traction–separation law can be expressed as the following equation, in which the crack opening can be obtained from the enhancement nodal displacements related to the enhanced degrees of freedom:

$$\mathbf{t}_{dl} = \mathbf{T}_{dl}\mathbf{w} = \mathbf{T}_{dl}\overline{\mathbf{N}}\ \mathbf{a}_{\mathbf{i}} \tag{28}$$

where $\mathbf{t}_{dl}$ is the traction in the l-th layer, $\mathbf{T}_{dl}$ is the tangent stiffness matrix of the traction–separation law for the l-th layer, $\mathbf{w}$ is the largest crack opening reached during the loading history, and $\mathbf{a}_i$ is the enhancement nodal displacement. For a cracked element, linear elastic material properties are still assumed in the continuous solid, but the enhancement internal force related to traction over the crack would decrease with the increase of the crack opening. In the cohesive interface the softening curve is governed by the fracture energy (G_f). A concrete bi-linear softening curve is used herein to describe the decrease of traction with the increase of the crack opening after cracking, as shown in Fig. 9, where f_t' is the tensile strength of concrete, t_{dn} is the traction normal to the crack, and w is the crack opening. As t_{dn} is not less than $0.2f_t'$ the relation between traction and opening is given as $t_{dn} = f_t' - 1.25\frac{f_t'^2}{G_f}w$, and after t_{dn} drops below $0.2f_t'$ the relation is given as $t_{dn} = 0.2f_t' - \frac{0.2}{6.16}\frac{f_t'^2}{G_f}(w - 0.64w_{ch})$ until the opening attains $0.68w_{ch}$ $\left(w_{ch} = \frac{G_f}{f_t'}\right)$. When the crack opening exceeds the traction-free open width $(0.68w_{ch})$, the tangent stiffness is set to zero.

Bazant and Becq-Giraudon [52] proposed the fracture energy at an ambient temperature as:

$$G_f(20\,^\circ\mathrm{C}) = 2.5\times\alpha_0\left(\frac{f_c'(20\,^\circ\mathrm{C})}{0.051}\right)^{0.46}\left(1+\frac{d_a}{11.27}\right)^{0.22}(Ratio_{w/c})^{-0.3} \tag{29}$$

where $\alpha_0 = 1.0$ for rounded aggregates and $\alpha_0 = 1.44$ for crushed or angular aggregates, d_a (in mm) is the maximum aggregate size, and $Ratio_{w/c}$ is the water-to-cement ratio. However, under fire conditions the fracture energy of concrete is expected to change at elevated temperatures. This should be taken into account in the current model. In order to extend the above model to the temperature-dependent cohesive model, the tensile strength (f_t') and fracture energy (G_f) in Fig. 9 should be temperature-related. The temperature-dependent tensile strength $f_t'(T)$ is calculated using the model specified in EN1992-1-2 [48], and the temperature-dependent fracture energy $G_f(T)$ is determined according to the CEB-FIP model code [53] as:

$$G_f(T) = G_f(20\,^\circ\mathrm{C})(1.06 - 0.003T) \tag{30}$$

where T is the temperature in °C. To replace G_f and f_t' with $G_f(T)$ and $f_t'(T)$ in Fig. 9 respectively, the temperature-dependent cohesive curve is obtained in the current model.

2.2. Reinforcing steel bar and bond-link elements

As shown in Fig. 1, a reinforced concrete beam is modelled as an assembly of plain concrete, reinforcing steel bar, and bond-link elements. Previously, a general 3D three-node beam column element was developed by the second author [54], which proved being able to model the reinforced concrete beams and reinforcement bars well. Note that both the 3-node beam element and 2-node element are compatible with the 4-node quadrilateral concrete element in modelling the reinforced concrete structures. For convenience purposes, the three-node beam element developed in [54] is employed in this paper to model the reinforcing steel bar. Each node of the

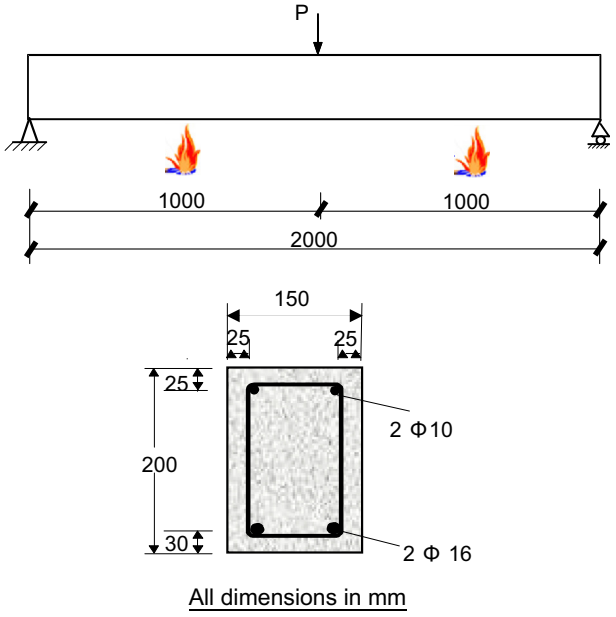

Fig. 12. Details of a simply supported reinforced concrete beam under ISO834 fire.

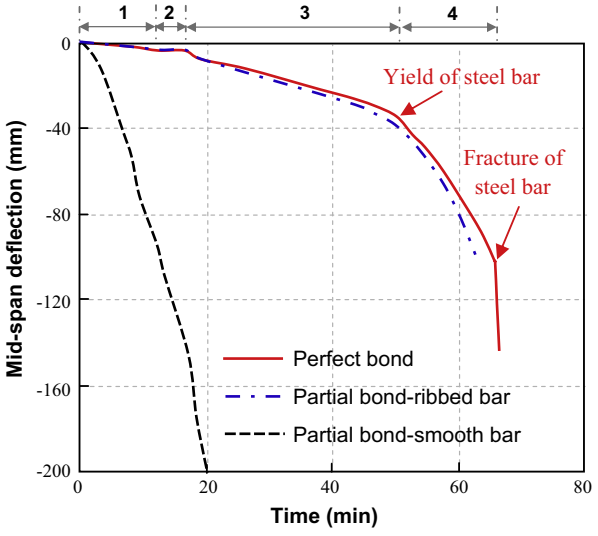

Fig. 13. Predicted mid-span deflections with time for different bond characteristics.

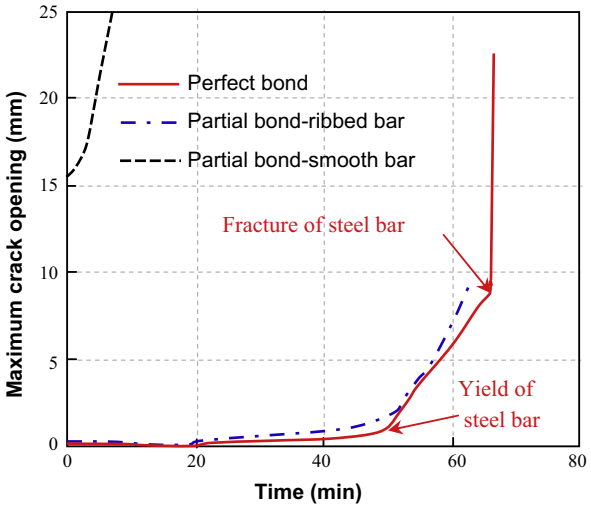

Fig. 14. Predicted maximum crack openings with time for different bond characteristics.

steel bar element contains the conventional six degrees of freedom (three translational and three rotational, in both local and global coordinates). As shown in Fig. 10, the steel mechanical properties and thermal elongation are calculated based on the models specified in EN1992-1-2 [48]. The beam column element allows the reference axis to be placed outside the cross-section. Thus, the reinforcing steel bars can be easily modelled using beam column elements, together with layered concrete elements, to simulate a reinforced concrete beam in fire.

At present there are several ways in which to model the concrete–reinforcement interface, such as the bond-link element and cohesive crack model using the enrichment function. However, the bond-link element has been widely used for structural analysis and design of reinforced concrete structures. Therefore, in order to model the bond characteristic between the concrete and reinforcing steel bar in fire, a two-node bond-link element developed by Huang [55] is employed in this research to link the nodes between a plain concrete element and reinforcing steel bar element. The bond-link element has no physical dimensions, and the two connected nodes originally occupy the same location in the finite element mesh of the undeformed structure. Three bond-link elements are used to connect two plain concrete elements with one 3-node steel bar element. Each node of the bond-link element includes three translational and three rotational degrees of freedom. It is, however, assumed that the slip between reinforcing steel and concrete is related only to the longitudinal axis direction of the steel bar element. The bond element is capable of modelling full, partial and zero bonds between the concrete and reinforcing steel within the reinforced concrete structures.

In order to investigate the mesh sensitivity of the current model a simply supported reinforced concrete beam at an ambient temperature was modelled using different meshes, i.e. 200 concrete

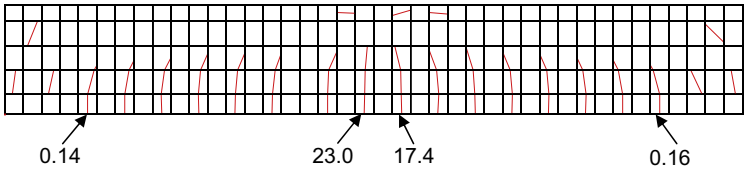

(a) Predicted cracking pattern (perfect bond)

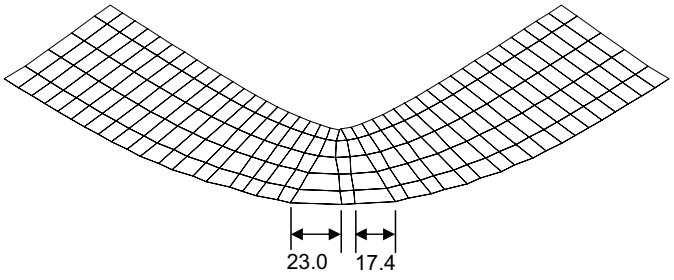

(b) Predicted deformed mesh (perfect bond, x-axis displacement has been amplified 5 times).

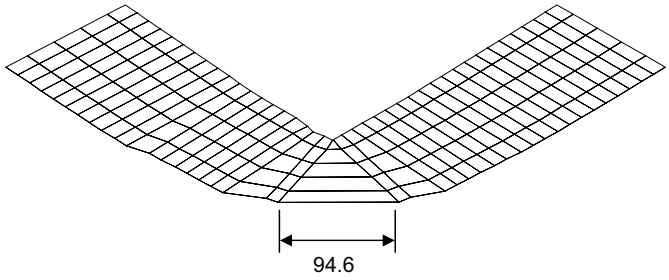

(c) Predicted deformed mesh (partial bond with smooth bars, x-axis displacement has been amplified 5 times).

Fig. 15. Predicted localised cracks of reinforced concrete beams in fire for different bond conditions (unit: mm).

elements plus 40 steel bar elements and 400 concrete elements plus 80 steel bar elements. The beam with a length of 2000 mm and a cross-sectional dimension of 150 mm in width and 200 mm in height is reinforced by two ribbed 16 mm (in diameter) tensile steel bars and two ribbed 10 mm (in diameter) compressive steel bars. The compressive strength of concrete at testing is 23.8 MPa. The yield strengths of the 16 mm (in diameter) bar and 10 mm (in diameter) bar are 406 MPa and 365 MPa, respectively. The beam was modelled under four-point loads. The comparison of predicted loads versus mid-span deflection by using different FE meshes is given in Fig. 11. It can be seen that the results are almost identical to each other. Therefore, the current model is not very mesh-sensitive.

3. Numerical example and validations

It is noted that under fire conditions the temperature distribution within the reinforced concrete beam may be significantly affected due to the formation of big localised cracks. In particular, some major cracks may result in the main reinforcing steel bars being directly exposed to fire. However, it is a difficult task to precisely predict the impact of localised cracks on the thermal behaviour of the beam in fire, and this is outside the scope of the current paper. According to the experimental investigations conducted recently by Ervine [56,57], in which the rate of thermal propagation through the undamaged beams was compared with the beams with minor cracking (surface crack opening was around 1 mm) and the beams with major cracking (surface crack opening up to around 5 mm), the effect of tensile cracking on the thermal propagation of the beam was not significant and could be ignored in structural analyses. Thus, in this paper, for simplicity, the impact of localised cracks on the thermal behaviour of the beam is not taken into account. However, previous research has indicated that the thermo-hygro-mechanical effect of concrete at a high temperature is significant, especially when concrete is spalled under fire conditions [58–62]. The second author of this paper successfully modelled the effects of concrete spalling on the thermal and structural behaviour of reinforced concrete slabs by using a layer procedure to allow some concrete layers to be "void" (with zero mechanical strength and stiffness; zero thermal resistance) [63]. This method can be easily incorporated into the current layered quadrilateral concrete element procedure to model the impact of concrete spalling. For modelling a reinforced concrete beam in fire, the first step of the analysis is to perform the thermal analyses on the beams modelled. Huang et al. [64] developed a two-dimensional nonlinear finite-element procedure (FPRCBC-T) to predict the temperature distributions within the cross-sections of reinforced concrete members subjected to a given fire time–temperature curve. In this study the program FPRCBC-T is used to obtain the temperature history across the section of reinforced concrete beams. The influence of moisture on the concrete is considered. However, the influence of concrete cracking on the temperature distribution is not included. The predicted temperature histories are then used to perform structural analysis for the reinforced concrete beams. The mesh of the cross-sections of the beams used for thermal analysis is also used for the structural analysis. It is assumed that changes in loads or temperatures occur only at the beginning of each time or temperature step. During each step the external loads and temperatures in the layers of all elements are assumed to remain constant.

3.1. A simply supported reinforced concrete beam in fire

As a numerical example, a simply supported reinforced concrete beam (subjected to ISO834 standard fire) was modelled to demonstrate the capability of the current model developed for capturing

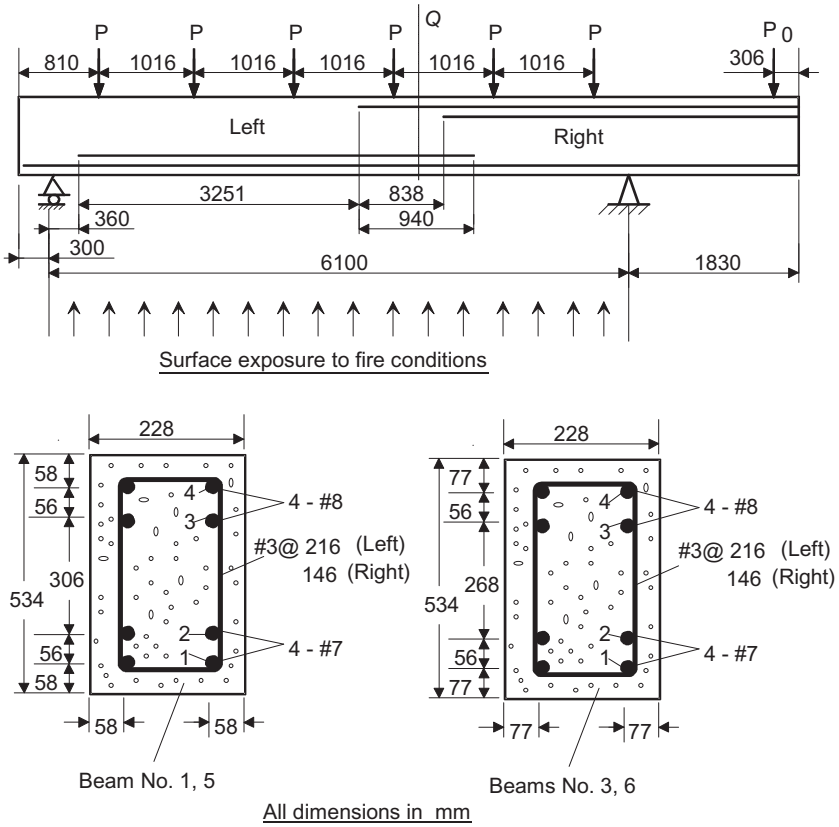

Fig. 16. Details of tested reinforced concrete beams in fires (adapted from [65]).

the localised fracture of reinforced concrete beams in fire. Fig. 12 shows the details of the modelled beam. The beam was reinforced by two ribbed 16 mm (in diameter) tensile steel bars and two ribbed 10 mm (in diameter) compressive steel bars. The compressive strength of concrete was 23.8 MPa. The yield strengths of the 16 mm (in diameter) bar and 10 mm (in diameter) bar were 406 MPa and 365 MPa respectively. The transverse point load at mid-span was 40 kN, which was kept constant during the fire. Three cases of a perfect bond, partial bond with ribbed steel bars, and partial bond with smooth steel bars were modelled.

Fig. 13 presents the predicted mid-span deflections of the beam against time for different bond characteristics. For the perfect bond case the deflection–time relation can be generally characterised as four stages before the beam reaches failure, as shown in Fig. 13. At stage 1, the deflection of the beam developed slowly, mainly due to the thermal bowing. The degradation of materials caused by rising temperatures was not remarkable in terms of strength and Young's modulus during this period. At stage 2, the deflection–time curve shows a flat segment from 13 min to 17 min. This is because the temperature of tensile reinforcing steel bars remained almost constant, due to the effect of free water evaporation within the concrete. At stage 3, the temperature of tensile steel bars rose from 120 °C to more than 500 °C, and the deflection rate was increased due to the remarkable deterioration of material strengths at high temperatures. After the tensile reinforcing steel bars yielded (at stage 4), the deflection of the beam increased significantly until the fracture of the steel bars at mid-span. It is obvious that the bond-slip characteristic, between the reinforcing steel bar and the concrete, has a significant influence on the behaviour of reinforced concrete beams in terms of fire resistance and deflection. For instance, the fire resistances of the perfect bond and ribbed bar cases were around 66 min and 62 min, respectively. However, the fire resistance of the smooth bar case was only 13 min.

Fig. 14 shows the predicted crack opening history at mid-span of the beam, in which the crack openings were calculated using Eq. (28). It was found that the crack opening at mid-span decreased slightly at the initial stage due to the effect of thermal expansion, and then the crack opening increased gradually. After the steel bars

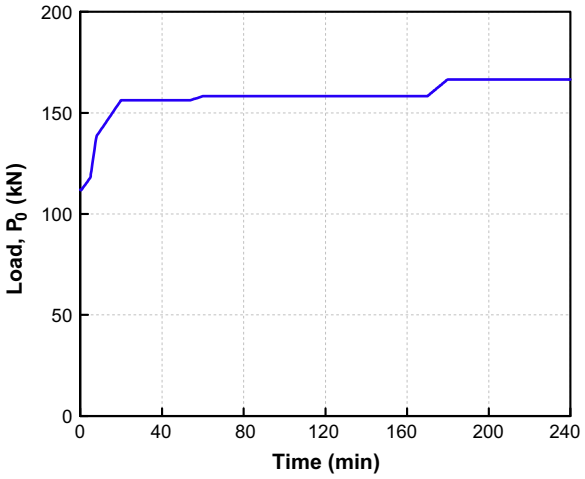

Fig. 17. History of load (P_0) at cantilever end (adapted from [65]).

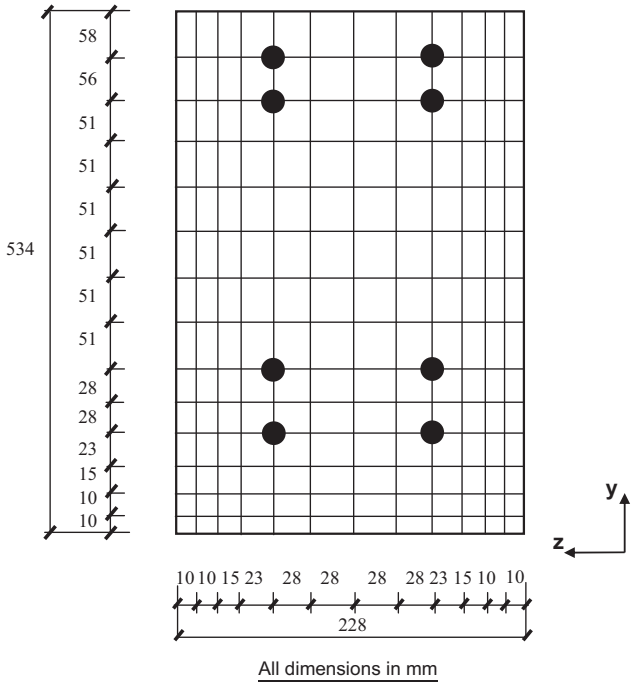

Fig. 18. The division of the cross-section of Beam 1 for the thermal analysis.

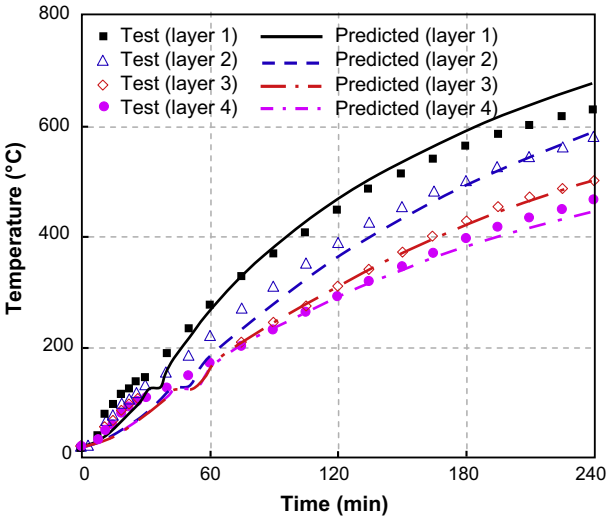

(a) Beam1 (ASTM fire)

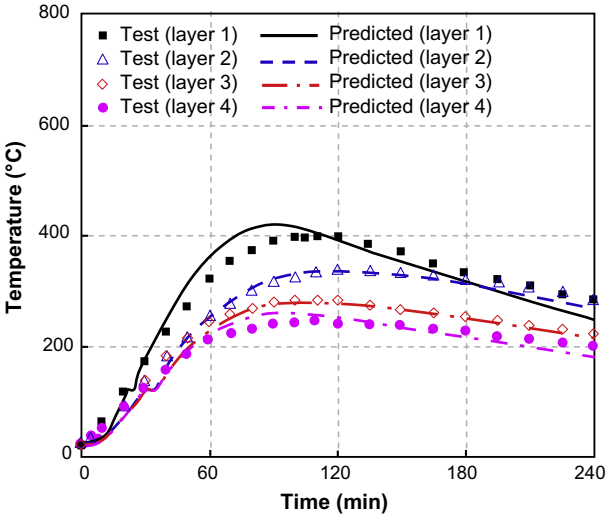

(b) Beam5 (SDHI fire)

Fig. 19. Comparison of predicted and measured temperatures of four main reinforcing steel bars of Beams 1 and 5.

yielded, the crack opening increased significantly until the fracture of the steel bars. It is obvious that the bond characteristic between the reinforcing steel bar and concrete has a significant influence on the maximum crack opening. Under the same fire exposure time, the opening of the ribbed bar case was greater than that of the perfect bond case, and the difference between the two cases became more significant after the tensile steel bars yielded. In the smooth bar case, its maximum crack opening had already exceeded 15 mm at the ambient temperature before the fire, and the crack opening of the smooth bar case increased dramatically at elevated temperatures.

The cracking pattern and deformed mesh of the beam, with a perfect bond condition at 66 min of fire time, are shown in Fig. 15(a) and (b). It can be seen that the XFEM developed in this paper can reasonably predict the formation and propagation of individual cracks. For the perfect bond case at 66 min of fire time, the openings of two major cracks at mid-span were 23.0 mm and 17.4 mm respectively. However, the cracks near the supports were only 0.14 mm and 0.16 mm, respectively. As shown in Fig. 15(c), for the smooth bar case, the maximum opening of the major crack at mid-span reached 94.6 mm. In both cases the mid-span elements appear obviously distorted, because the mesh held a very big localised crack. It is evident that the model proposed is able to capture the localised fracture of reinforced concrete beams under fire conditions very well.

3.2. Fire tests of reinforced concrete beams

In order to validate the model proposed in this paper, four reinforced concrete beams subjected to fire tests were modelled herein. These fire tests on normal-strength reinforced concrete beams with ribbed steel bars were conducted by Lin et al. [65]. For these tests, two heating curves, the ASTM fire and Short Duration High Intensity (SDHI) fire, were adopted. Here the four beams, designated as Beams 1, 3, 5 and 6, were modelled. Beams 1 and 3 were heated using the ASTM fire, and Beams 5 and 6 were subjected to the SDHI fire. Fig. 16 provides details of Beams 1, 3, 5 and 6, where the load P was kept constant at 44.48 kN during each fire

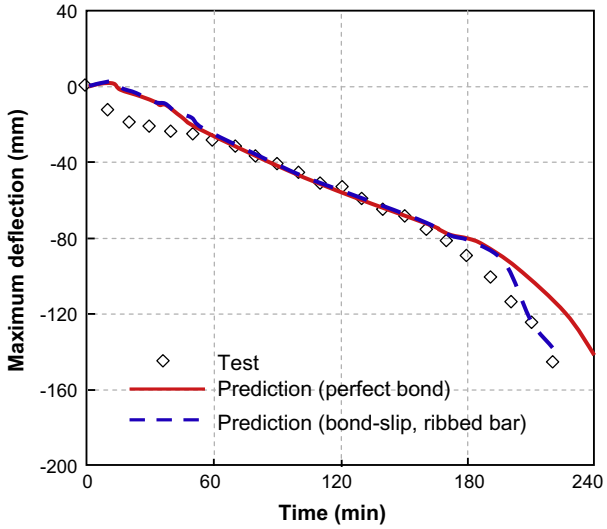

Fig. 20. Comparison of predicted and measured maximum deflections of Beam 1 (ASTM fire).

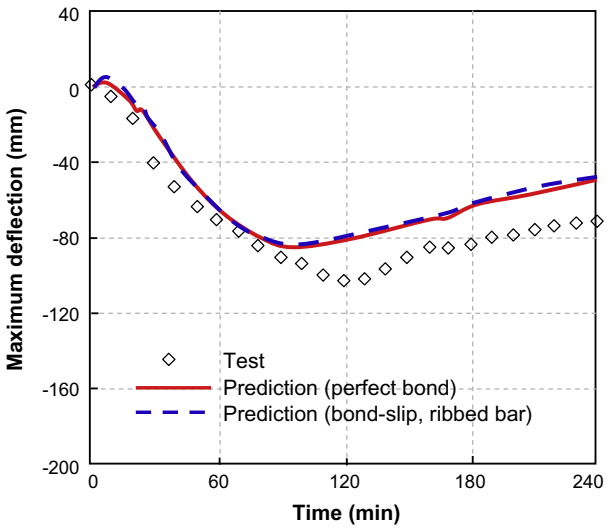

Fig. 22. Comparison of predicted and measured maximum deflections of Beam 5 (SDHI fire).

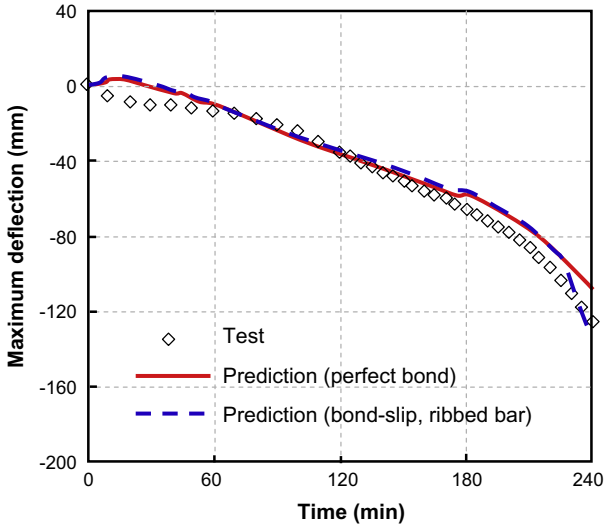

Fig. 21. Comparison of predicted and measured maximum deflections of Beam 3 (ASTM fire).

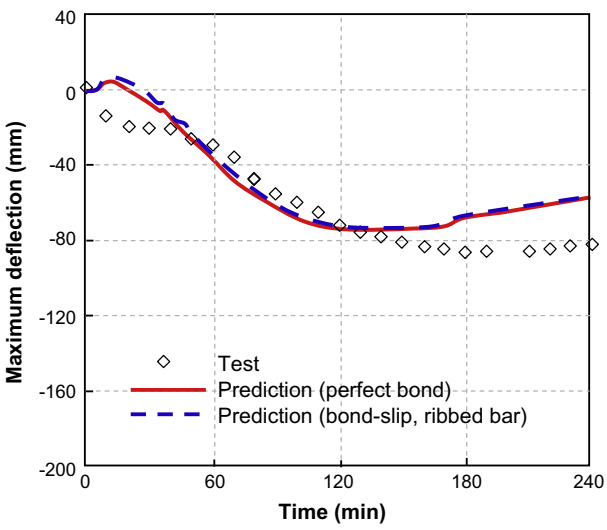

Fig. 23. Comparison of predicted and measured maximum deflections of Beam 6 (SDHI fire).

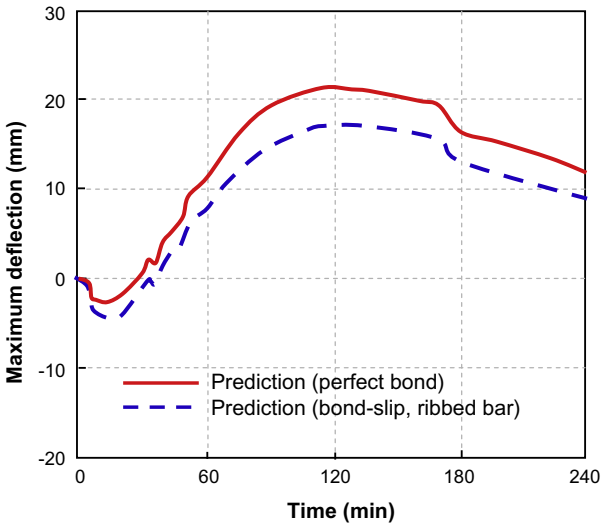

Fig. 24. Comparison of predicted deflections at the cantilever end of Beam 6 (SDHI fire).

test, although the cantilever force P_o varied as the test progressed. The history of the cantilever force P_o is illustrated in Fig. 17. The measured material properties at room temperature were the: concrete's compressive strengths: $f'_c(20\,^\circ\text{C}) = 27.86$ MPa (Beam 1), $f'_c(20\,^\circ\text{C}) = 31.5$ MPa (Beam 3), $f'_c(20\,^\circ\text{C}) = 33.73$ MPa (Beam 5), $f'_c(20\,^\circ\text{C}) = 34.54$ MPa (Beam 6), and steel yield strengths: $f_t(20\,^\circ\text{C}) = 487.27$ MPa (bar #7), and $f_t(20\,^\circ\text{C}) = 509.54$ MPa (bar #8). Those tested material properties were used for the validations.

The tested beams were subjected to three-face heating from its bottom and two sides. For the thermal analysis the cross-section of beams is divided, as 12 columns by 14 rows, with a total of 168 segments. This means that each concrete element was divided into 12 layers for the structural analysis. As an example, Fig. 18 shows the division of the cross-section of Beam 1, where the size of the concrete segments close to the fire boundary is less than that of the concrete segments away from the fire. Fig. 19 illustrates the predicted temperatures, together with tested results for four main reinforcing steel bar layers of Beams 1 and 5, where the reinforcing steel layers are denoted in sequence from bottom to top as Layers 1–4 (see Fig. 16). It is evident that good agreement has been achieved between the tests and predictions. The temperature histories obtained in the thermal analysis were subsequently used for the structural analyses of the beams.

In the analysis, each beam was modelled as an assembly of 1652 (14×118) layered quadrilateral plain concrete elements, 146 steel bar beam elements, and 296 bond-link elements. The mesh sensitivity test was conducted before the analysis, where the doubly finer mesh was used for the comparison. The results of the current mesh and the finer mesh were almost identical to each other. It is evident that the predicted results are not sensitive to the element size under the current mesh used. The predicted maximum vertical deflections for Beams 1, 3, 5 and 6, against time, are presented in Figs. 20–23. The maximum vertical deflections of all beams appeared at a position about 3500 mm away from the right-hand side support (see Fig. 16). It is evident that the predictions of the developed model agree reasonably well with the test results for the four beams in terms of deflections. It was found that the beams showed small upward deflections at the initial stage of the fire. This was due to the fact that the cantilever force P_o kept increasing at the initial stage (see Fig. 17), which tended to result in the downward deflection at the cantilever end, and the corresponding upward deflection at the first bay of beams. Afterwards, when P_o was kept stable, the beams developed downward deflections due to the influence of elevated temperatures.

From Figs. 20 and 21 it can be seen that for Beams 1 and 3 there is no obvious difference between the ribbed bar case and perfect bond case in terms of deflections until the later stage of fire. Two predicted deflection curves diverted: after 180 min for Beam 1, and 225 min for Beam 3. It is evident that the bond characteristics have a considerable influence on these two beams in terms of the deflections at the later stages of a fire. Generally, compared to the perfect bond case, the predicted deflections by the ribbed bar case agreed better with the test results. Therefore, if a perfect bond condition is assumed for modelling the interaction between reinforcing steel bars and concrete, the predicted results may be on the unconservative side.

The results of Beams 5 and 6 are respectively shown in Figs. 22 and 23. It can be seen that the effect of bond characteristics on the deflection of the mid-span areas of the beams is relatively small, compared to Beams 1 and 3. This is due to the fact that these beams were subjected to a Short Duration High Intensity (SDHI) fire, and the maximum temperatures of the reinforcing steel bar did not exceed 400 °C (see Fig. 19). It is also interesting to see that the deflection of the ribbed bar case is even slightly smaller than that of the perfect bond case. This is owing to the fact that the ribbed bar case has slightly bigger upward deflections than the

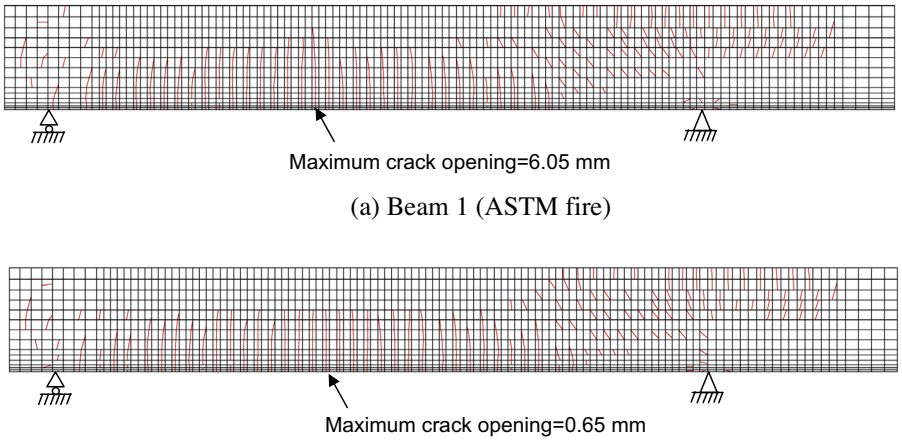

Fig. 25. Predicted cracking patterns of Beams 1 and 5.

perfect bond case at the initial stages of the fire. However, from the deflection of the cantilever end (shown in Fig. 24) for Beam 6, it can be seen that bond conditions have a more significant influence on the continuous support than the mid-span areas of the beam.

Fig. 25(a) and (b) present the predicted cracking patterns of Beams 1 and 5, respectively. It is evident that the current model can predict the formation and propagation of individual cracks quite well. The predicted crack patterns are reasonable where the flexural cracks caused by a sagging moment distribute at the lower part of mid-span areas, whilst the flexural cracks caused by a hogging moment distribute at the upper part over the continuous support. Besides that, diagonal cracks were also found within the reinforced concrete beam. The maximum crack opening of Beam 1 attained 6.05 mm near the mid-span, and the maximum crack opening of Beam 5 reached 0.65 mm only due to the Short Duration High Intensity (SDHI) fire applied.

4. Conclusions

In this paper a robust layered finite element procedure is proposed for modelling the localised fracture of reinforced concrete beams at elevated temperatures. In this new model the plain concrete is modelled by 4-node layered quadrilateral elements, incorporated into the extended finite element method (XFEM). The element is divided into layers to take into account the temperature distribution over the cross-section of the beam. Additional degrees of freedom are used to describe a discontinuous displacement field, and the enhancement function is used to realise the displacement jump over a crack for the cracked elements. A criterion based on a weighted average stress approach is proposed to determine the initiation of individual cracks within the plain concrete elements. The complications of structural behaviour under fire conditions, such as thermal expansion, the bond characteristic between reinforcing steel bars, concrete at elevated temperatures, and the change of material properties with temperature, are all considered in the model.

The new model has been validated against previous fire test results on reinforced concrete beams. A numerical example of modelling a simply supported reinforced concrete beam (subjected to ISO834 fire) has been analysed to demonstrate the capability of the current model for capturing the localised fracture of reinforced concrete beams under fire conditions. It has been shown that the XFEM nonlinear procedure proposed can predict the global response of reinforced concrete beams with good accuracy. The formation and propagation of individual cracks within the beams are also modelled, capturing the localised fracture, and predicting crack openings during the analysis. The model developed in this paper provides an excellent numerical approach for assessing both structural stability (global behaviour) and integrity (localised fracture) of reinforced concrete members in fire. The model proposed here will be further extended to 3D modelling of localised fracture of reinforced concrete slabs under fire conditions in order to assess the integrity failure of concrete floor slabs.

Acknowledgement

The authors gratefully acknowledge the support of the Engineering and Physical Sciences Research Council of Great Britain under Grant No. EP/I031553/1.

References

[1] Bailey CG, Toh WS. Small-scale concrete slab tests at ambient and elevated temperatures. Eng Struct 2007;29(10):2775–91.
[2] Foster SJ. Tensile membrane action of reinforced concrete slabs at ambient and elevated temperatures. Ph.D. Thesis. Department of Civil and Structural Engineering, University of Sheffield; 2006.
[3] Foster SJ, Bailey CG, Burgess IW, Plank RJ. Experimental behaviour of concrete floor slabs at large displacement. Eng Struct 2004;26(9):1231–47.
[4] Wang Y, Dong YL, Zhou GC. Nonlinear numerical modeling of two-way reinforced concrete slabs subjected to fire. Comput Struct 2013;119(4):23–36.
[5] Davie CT, Zhang HL, Gibson A. Investigation of a continuum damage model as an indicator for the prediction of spalling in fire exposed concrete. Comput Struct 2012;94–95(3):54–69.
[6] Chung JH, Consolazio GR, McVay MC. Finite element stress analysis of a reinforced high-strength concrete column in severe fires. Comput Struct 2006;84(8):1338–52.
[7] Capua DD, Mari AR. Nonlinear analysis of reinforced concrete cross-sections exposed to fire. Fire Saf J 2007;42(2):139–49.
[8] Kodur VKR, Dwaikat M. A numerical model for predicting the fire resistance of reinforced concrete beams. Cem Concr Compos 2008;30(5):431–43.
[9] Riva P, Franssen JM. Non-linear and plastic analysis of RC beams subjected to fire. Struct Concr 2008;9(1):30–43.
[10] Izzuddin BA, Elghazouli AY. Failure of lightly reinforced concrete members under fire. I: Analytical modelling. J Struct Eng ASCE 2004;130(1):3–17.
[11] Huang ZH, Burgess IW, Plank RJ. Nonlinear analysis of reinforced concrete slabs subjected to fires. ACI Struct J 1999;96(1):127–35.
[12] Huang ZH, Burgess IW, Plank RJ. Modelling membrane action of concrete slabs in composite buildings in fire. Part I: Theoretical development. J Struct Eng ASCE 2003;129(8):1093–102.
[13] Bratina S, Čas B, Saje M, Planinc I. Numerical modelling of behaviour of reinforced concrete columns in fire and comparison with Eurocode 2. Int J Solids Struct 2005;42(10):5715–33.
[14] Gao WY, Dai JG, Teng JG, Chen GM. Finite element modeling of reinforced concrete beams exposed to fire. Eng Struct 2013;52(7):488–501.
[15] Belytschko T, Black T. Elastic crack growth in finite elements with minimal remeshing. Int J Numer Meth Eng 1999;45(5):601–20.
[16] Moës N, Dolbow J, Belytschko T. A finite element method for crack growth without remeshing. Int J Numer Meth Eng 1999;46(1):131–50.
[17] Melenk JM, Babuška I. The partition of unity finite element method: basic theory and application. Comput Meth Appl Mech Eng 1996;139(1–4):289–314.
[18] Wells GN, Sluys LJ. A new method for modelling cohesive cracks using finite elements. Int J Numer Meth Eng 2001;50(12):2667–82.
[19] Zi G, Belytschko T. New crack-tip elements for XFEM and applications to cohesive cracks. Int J Numer Meth Eng 2003;57(15):2221–40.
[20] Verhoosel CV, Remmers JJC, Gutiérrez MA. A dissipation-based arc-length method for robust simulation of brittle and ductile failure. Int J Numer Meth Eng 2009;77(9):1290–321.
[21] Moës N, Belytschko T. Extended finite element method for cohesive crack growth. Eng Fract Mech 2002;69(7):813–33.
[22] Hansbo A, Hansbo P. A finite element method for the simulation of strong and weak discontinuities in solid mechanics. Comput Methods Appl Mech Eng 2004;193(33–35):3523–40.
[23] Budyn É, Zi G, Moës N, Belytschko T. A method for multiple crack growth in brittle materials without remeshing. Int J Numer Meth Eng 2004;61(10):1741–70.
[24] Daux C, Moës N, Dolbow J, Sukumar N, Belytschko T. Arbitrary branched and intersecting cracks with the extended finite element method. Int J Numer Meth Eng 2000;48(12):1741–60.
[25] Réthoré J, Gravouil A, Combescure A. An energy-conserving scheme for dynamic crack growth using the extended finite element method. Int J Numer Meth Eng 2005;63(5):631–59.
[26] Duan Q, Song JH, Menouillard T, Belytschko T. Element-local level set method for three-dimensional dynamic crack growth. Int J Numer Meth Eng 2009;80(12):1520–43.
[27] Bordas S, Nguyen PV, Dunant C, Guidoum A, Nguyen-Dang H. An extended finite element library. Int J Numer Meth Eng 2007;71(6):703–32.
[28] Talebi H, Silani M, Bordas S, Kerfriden P, Rabczuk T. A computational library for multiscale modeling of material failure. Comput Mech 2014;53(5):1047–71.
[29] Natarajan S, Bordas S, Mahapatra DY. Numerical integration over arbitrary polygonal domains based on Schwarz–Christoffel conformal mapping. Int J Numer Meth Eng 2009;80(1):103–34.
[30] Bordas S, Rabczuk T, Hung NX, Nguyen VP, Natarajan S, Bog T, et al. Strain smoothing in FEM and XFEM. Comput Struct 2010;88(23–24):1419–43.
[31] Chen L, Rabczuk T, Bordas SP, Liu G, Zeng K, Kerfriden P. Extended finite element method with edge-based strain smoothing (ESm-XFEM) for linear elastic crack growth. Comput Methods Appl Mech Eng 2012;209–212(2):250–65.
[32] Vu-Bac N, Nguyen-Xuan H, Chen L, Bordas S, Kerfriden P, Simpson RN, et al. A node-based smoothed extended finite element method (NS-XFEM) for fracture analysis. Comput Model Eng Sci 2011;73(4):331–56.
[33] Bordas S, Natarajan S, Kerfriden P, Augarde CE, Mahapatra DR, Rabczuk T, et al. On the performance of strain smoothing for quadratic and enriched finite element approximations (XFEM/GFEM/PUFEM). Int J Numer Meth Eng 2011;86(4–5):637–66.
[34] Dias-da-Costa D, Alfaiate J, Sluys LJ, Areias P, Júlio E. An embedded formulation with conforming finite elements to capture strong discontinuities. Int J Numer Meth Eng 2013;93(2):224–44.
[35] Simoni L, Schrefler BA. Multi field simulation of fracture. Adv Appl Mech 2014;47:367–519 [chapter 4 (Editor: S. Bordas)].
[36] Rabczuk T, Bordas S, Zi G. On three-dimensional modelling of crack growth using partition of unity methods. Comput Struct 2010;88(23–24):1391–411.

[37] Nguyen VP, Rabczuk T, Bordas S, Duflot M. Meshless methods: a review and computer implementation aspects. Math Comput Simulat 2008;79(3):763–813.
[38] Bordas S, Rabczuk T, Zi G. Three-dimensional crack initiation, propagation, branching and junction in non-linear materials by extrinsic discontinuous enrichment of meshfree methods without asymptotic enrichment. Eng Fract Mech 2008;75(5):943–60.
[39] Bordas S, Zi G, Rabczuk T. Three-dimensional non-linear fracture mechanics by enriched meshfree methods without asymptotic enrichment. In: Combescure A, Borst RD, Belytschko T, editors. IUTAM symposium on discretization methods for evolving discontinuities, chapter: meshless finite element methods. Springer; 2007. p. 21–36.
[40] Rabczuk T, Zi G, Bordas S, Nguyen-Xuan H. A geometrically non-linear three dimensional cohesive crack method for reinforced concrete structures. Eng Fract Mech 2008;75(16):4740–58.
[41] Xiao QZ, Dhanasekar M. Plane hybrid stress elements for 3D analysis of moderately thick solids subjected to loading symmetric to midsurface. Int J Solids Struct 2007;44(7–8):2458–76.
[42] Ahmed A. Extended finite element method (XFEM)-modeling arbitrary discontinuities and failure analysis. Master Thesis, Italy: University of Pavia; 2009.
[43] Bathe KJ. Finite element procedures. New Jersey: Prentice-Hall Inc.; 1996.
[44] Liao FY, Huang ZH. A nonlinear procedure for modelling localized fracture of reinforced concrete structures. Report No. SED-DCE-2003-1, UK: Brunel University; 2013.
[45] Xiao QZ, Karihaloo BL. Improving the accuracy of XFEM crack tip fields using higher order quadrature and statically admissible stress recovery. Int J Numer Meth Eng 2006;66(9):1378–410.
[46] Barzegar-Jamshidi F. Nonlinear finite element analysis of reinforced concrete under short term monotonic loading. Ph.D. Thesis, University of Illinois at Urbana-Champaign; 1987.
[47] Kupfer HB, Gerstle KH. Behavior of concrete under biaxial stresses. J Eng Mech Div ASCE 1973;99(EM4):853–66.
[48] EN 1992-1-2. Eurocode 2, design of concrete structures, Part 1.2: General rules – structural fire design. Brussels: Commission of the European Communities; 2004.
[49] American Society of Civil Engineers. Finite element analysis of reinforced concrete. New York; 1982.
[50] Hillerborg A, Modeer M, Petersson PE. Analysis of crack formation and crack growth in concrete by means of fracture mechanics and finite elements. Cem Concr Res 1976;6(6):773–82.
[51] Karihaloo BL, Xiao QZ. Asymptotic fields at the tip of a cohesive crack. Int J Fract 2008;150(1–2):55–74.
[52] Bažant ZP, Becq-Giraudon E. Statistical prediction of fracture parameters of concrete and implications for choice of testing standard. Cem Concr Res 2002;32(4):529–56.
[53] CEB-FIP Model Code: Committee Euro-International du Beton. Bulletin D'information No. 213/214. Tomas Telford (London); May 1993.
[54] Huang ZH, Burgess IW, Plank RJ. Three-dimensional analysis of reinforced concrete beam–column structures in fire. J Struct Eng ASCE 2009;135(10):1201–12.
[55] Huang ZH. Modelling the bond between concrete and reinforcing steel in a fire. Eng Struct 2010;32(11):3660–9.
[56] Ervine A. Damaged reinforced concrete structures in fire. Ph.D. Thesis. Department of Civil and Structural Engineering, University of Edinburgh; 2012.
[57] Ervine A, Gillie M, Stratford TJ, Pankaj P. Thermal propagation through tensile cracks in reinforced concrete. J Mater Civ Eng 2012;24(5):516–22.
[58] Baggio P, Majorana CE, Schrefler BA. Thermo-hygro-mechanical analysis of concrete. Int J Numer Meth Fl 1995;20(6):573–95.
[59] Bažant ZP. Analysis of pore pressure, thermal stress and fracture in rapidly heated concrete. In Phan LT, Carino NJ, Duthinh D, Garboczi E, editors. International workshop on fire performance of high-strength concrete. Gaithersburg (MD); 1997. p. 155–64.
[60] Kodur VKR, Dwaikat MB. Hydro thermal model for predicting fire-induced spalling in concrete structural systems. Fire Saf J 2009;44(3):425–34.
[61] Mindeguia JC, Pimienta P, Carré H, Borderie CL. Experimental analysis of concrete spalling due to fire exposure. Eur J Environ Civ Eng 2013;17(6):453–66.
[62] Kukla, K. Concrete at high temperatures: hygro-thermo-mechanical degradation of concrete. Ph.D. Thesis. School of Engineering, University of Glasgow; 2010.
[63] Huang ZH. The behaviour of reinforced concrete slabs in fire. Fire Saf J 2010;45(5):271–82.
[64] Huang ZH, Platten A, Roberts J. Non-linear finite element model to predict temperature histories within reinforced concrete in fires. Build Environ 1996;31(2):109–18.
[65] Lin TD, Ellingwood B, Piet O. Flexural and shear behaviour of reinforced concrete beams during fire tests. Report no. NBS-GCR-87-536, Center for Fire Research, National Bureau of Standards; 1987.